

Force decomposition on flapping flexible plate via impulse theory and dynamic mode decomposition

Cite as: Phys. Fluids **35**, 101914 (2023); doi: [10.1063/5.0169989](https://doi.org/10.1063/5.0169989)

Submitted: 31 July 2023 · Accepted: 6 October 2023 ·

Published Online: 27 October 2023











View Online



Export Citation



CrossMark

Linlin Kang (康林林),¹  Shiyong Xiong (熊诗颖),^{2,a)}  Buchen Wu (吴步晨),^{3,a)}  Chao Li (李超),⁴ 
Mingming Ge (葛明明),¹  Dehan Yuan (袁德瀚),¹  Fei Han (韩非),¹  and Weicheng Cui (崔维成)¹ 

AFFILIATIONS

¹Key Laboratory of Coastal Environment and Resources of Zhejiang Province, School of Engineering, Westlake University, Hangzhou, Zhejiang 310030, China

²Department of Engineering Mechanics, School of Aeronautics and Astronautics, Zhejiang University, Hangzhou, Zhejiang 310027, China

³Department of Mechanical Engineering, National University of Singapore, Singapore 119260, Singapore

⁴Department of modern Mechanics, University of Science and Technology of China, Hefei, Anhui 230026, China

^{a)}Authors to whom correspondence should be addressed: shiyong.xiong@zju.edu.cn and buchenwu@u.nus.edu

ABSTRACT

Dynamic mode decomposition (DMD) is a widely used method to extract dynamic information from sequential flow data, aiding our comprehension of fluid dynamics and transport processes. While DMD can unveil internal system laws and predict unsteady flow phenomena, the connection between DMD modes and the nonlinear hydrodynamic behavior of solid bodies remains unexplored. This study investigated the internal relationship between DMD modes and their impact on hydrodynamic forces. We employed a penalty-immersed boundary method to simulate the behavior of a flapping flexible plate in a uniform incoming flow, generating extensive datasets of vorticity fields. By applying DMD to these datasets, we identified key modes governing the flow dynamics, including the shear layer, symmetric vortex street, and antisymmetric vortex street. Furthermore, we utilized the impulse theory to analyze the force characteristics of the plate based on the corresponding DMD modes. The net force is determined by the combined contributions of the impulse force and the vortex force. Our findings reveal that the net horizontal force is primarily influenced by the first two modes. Specifically, mode 1, characterized by a dimensionless frequency of $f^* = 0$, contributes to thrust, whereas mode 2, with $f^* = 1$, contributes to drag. This physical investigation holds relevance for fluid–structure systems involving the interaction dynamics of flexible structures with unsteady wake vortex systems.

Published under an exclusive license by AIP Publishing. <https://doi.org/10.1063/5.0169989>

I. INTRODUCTION

The advancement of computational fluid dynamics and flow measurement techniques has revolutionized the characterization of flow, achieving unprecedented levels of precision. As a result, there is a growing focus on extracting modal information from vast amounts of flow field data and modeling complex dynamic behaviors in fluid dynamics research. Dynamic mode decomposition (DMD), a pioneering method that couples spatial and temporal dynamics, has gained rapid recognition and widespread adoption.¹ The DMD method analyzes the dominant characteristics of unsteady flows, and these dominant modes can be effectively utilized to construct reduced-order models for accurately predicting the nonlinear dynamics of complex systems.

The DMD method's ability to decouple nonlinear flow behaviors with different frequency components has made it highly valuable in analyzing a wide range of flow problems. For example, it has been successfully applied in studying pitching foils,² flow control,^{3–5} biological self-propulsion,⁶ vortex-induced vibration,⁷ and turbulent boundary layer interaction.⁸ Nonetheless, there is a paucity of research concerning hydro/aerodynamic force mechanisms,^{9,10} particularly in the context of unsteady fluid–structure interaction systems.

While we often use the conventional surface stress integration formula to predict forces acting on solid objects, existing theories fall short of specifying which modes among the flow structures generated by object motion are the primary contributors to the overall force. On the other hand, employing DMD for the analysis of force mechanisms

offers distinct advantages, particularly in elucidating the influence of individual modes on a body. By identifying the pivotal modes that influence a body's forces, it can facilitate precise control of dynamic systems. Furthermore, our goal is to demonstrate the efficacy of DMD as a predictive tool by delving into the relationship between DMD modes and force generation.

In addition, some classical vorticity dynamic theories can be incorporated into the study of forces. Burgers¹¹ introduced the classical impulse theory, which was later developed independently by Wu¹² and Lighthill.¹³ This theory establishes a connection between forces and the rate of vorticity moment change in viscous flow. In a similar way, Chang¹⁴ developed a diagnostic force theory aimed at separating potential forces, such as added mass and inertial forces, and determining the contributions of individual fluid elements to these forces. Building on the classical impulse theory, Noca *et al.*¹⁵ extended the analysis domain to arbitrary finite domain. Wu *et al.*¹⁶ derived more unconventional force expressions by employing derivative-moment transformations. These transformations enable the substitution of the original integrand with the spatial derivative moments, which can be represented by other terms in the differential motion equations, when necessary. This approach explicitly reveals the impact of various local dynamic processes and structures on the integrated performance. Kang *et al.*¹⁷ further proposed a minimum-domain impulse theory to relate the whole force on the body to a limited flowfield region without the need for surface integrals along the outer domain boundary. Li and Wu¹⁸ made progress in this aspect by developing vortex force maps that connect the force generated by a vortex to corresponding position and velocity. Consequently, these theories have found successful application in analyzing local dynamic processes in scenarios such as bluff-body flows and insect flight.^{19,20}

Building upon prior research on the relationship between vortical structures and dynamics, this paper intends to conduct a force analysis of the vorticity field by incorporating DMD. Specifically, we use vorticity as the observed quantity for DMD decomposition, which has the following two main advantages: (1) Compared with velocity field and pressure field, the perturbation of vorticity field is exponentially decayed with distance. For the external-flow problem, it is only distributed near the object and in a limited area of the wake region. (2) Using impulse theory, the force on a body can be expressed as an integral function of vorticity and position, the contribution to the force of the body can realize the decomposition of both the region^{17,19,20} and the function (like the DMD decomposition), thus making it possible to predict the contribution of each DMD mode to the force by vorticity alone.

This paper focuses on the study of fish swimming, a flow characterized by a series of complex fluid-structure interactions and distinct characteristic frequencies. Numerous studies have revealed the impact of these frequencies on propulsion performance.^{21–24} Furthermore, some studies have delved deeper into exploring the relationship between the flow field surrounding the fish and the forces exerted on the fish's body.^{25,26} Inspired by previous research, we employ a flexible flapping plate as a model and combine the DMD method with the impulse theory to study the flow phenomena of fish swimming with the impulse theory.

We used a penalty-immersed boundary method for simulation to obtain the full-order vorticity field information of the flexible flapping plate problem, and utilized DMD method to extract the key modes

information of vorticity field evolution, from which we identified three types of wake vortex structures for all modes. We used impulse theory to evaluate the key modes that affect the force of the plate and explored the underlying physical mechanisms. The purpose of this study is to achieve an improved understanding of some of the fundamental mechanisms relevant to the DMD. The physical investigation is general for any fluid-structure system involving the interaction dynamics of flexible structures with an unsteady wake–vortex system.

The paper is organized as follows: In Sec. II, we give an overview of the problem set-up, including the governing equations for fluid dynamics and plate motion, details about the numerical solver for the coupled fluid-structure system along with its validation, and an introduction to DMD. The discussion regarding the forces associated with local vortical structures can be found in Sec. III. In Sec. IV, the DMD analysis for vortical flow over a plate and the force contributions from the decomposed modes are discussed. Finally, concluding remarks are provided in Sec. V.

II. COMPUTATIONAL MODEL

In this section, we begin by introducing the physical model and the numerical simulation method, followed by an introduction to the DMD method for analyzing flow field data.

A. Physical problem and mathematical formulation

A schematic of a flexible flapping plate heaving in a uniform flow with incoming velocity U_∞ is shown in Fig. 1. The heaving motion of the leading edge is described as

$$x_L(t) = 0, \quad y_L(t) = A \cos(2\pi f_c t), \quad (1)$$

where $A = 0.5L$ is the flapping amplitude, L is the length of the plate, f_c is the flap frequency, t is the time, and (x_L, y_L) is the position of the leading edge of the plate. The x-coordinate of the leading edge of the plate is zero. The trailing edge of the plate is free.

The motion of the fluid is governed by the incompressible viscous Navier–Stokes (NS) equations,

$$\frac{\partial \mathbf{u}}{\partial t} + \mathbf{u} \cdot \nabla \mathbf{u} = -\frac{1}{\rho} \nabla p + \frac{\mu}{\rho} \nabla^2 \mathbf{u} + \mathbf{f}, \quad (2)$$

$$\nabla \cdot \mathbf{u} = 0. \quad (3)$$

Here, $\mathbf{u} = (u, v)$ represents the fluid velocity, with u and v denoting the x-component and y-component of velocity, respectively. ρ is the fluid density, p is the pressure, μ is the dynamic viscosity, and \mathbf{f} is the body force term.

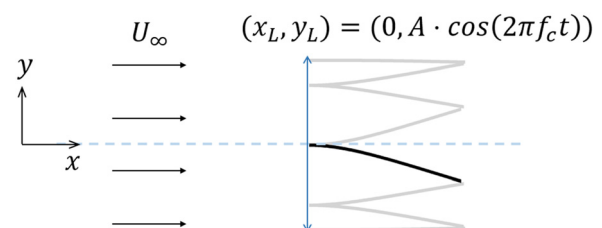


FIG. 1. Schematic diagram of a flexible plate heaving in a uniform flow with incoming velocity U_∞ . The plate is represented by a beam model, which is forced to flapping sinusoidally. (x_L, y_L) is the position of the leading edge of the plate.

The motion and deformation of the plate are described in a Lagrangian coordinate system. The governing structure equation is

$$\rho_s h \frac{\partial^2 \mathbf{X}}{\partial t^2} = \mathbf{F}_S + \frac{\partial}{\partial s} \left[Eh \left(1 - \left| \frac{\partial \mathbf{X}}{\partial s} \right|^{-1} \right) \frac{\partial \mathbf{X}}{\partial s} - \frac{\partial}{\partial s} \left(EI \frac{\partial^2 \mathbf{X}}{\partial s^2} \right) \right], \quad (4)$$

where $\rho_s h$ is the structural linear mass density of the plate, s is the Lagrangian coordinate along the plate, \mathbf{X} is the position of the plate, and \mathbf{F}_S is the Lagrangian force exerted on the plate by surrounding fluid. Eh and EI are the structural stretching rigidity and bending rigidity, respectively. At the leading edge of the plate, we have $\mathbf{X} = (0, y_L)$, $\partial \mathbf{X} / \partial s = \mathbf{e}_x$, $-Eh(1 - |\partial \mathbf{X} / \partial s|^{-1}) \partial \mathbf{X} / \partial s + EI \frac{\partial^3 \mathbf{X}}{\partial s^3} = \mathbf{0}$. At the trailing edge, the boundary conditions are $|\partial \mathbf{X} / \partial s|^{-1} = 1$, $\partial^2 \mathbf{X} / \partial s^2 = \mathbf{0}$, $\partial^3 \mathbf{X} / \partial s^3 = \mathbf{0}$, which mean that there are no tension force, bending moment and shearing force acting at the free end.

The reference quantities density ρ , velocity $U_{ref}(=Lf_c)$ and the length L are chosen to normalize the above equations. The key non-dimensional parameters are the Reynolds number $Re = \rho U_{ref} L / \mu$, the bending coefficient $K = EI / \rho U_{ref}^2 L^3$, the tension coefficient $S = Eh / \rho U_{ref}^2 L$, and the mass ratio of the plate to the fluid $M = \rho_s h / \rho L$.

B. Numerical method for fluid-plate interaction

We now summarize our numerical method to simulate the coupled fluid-plate interaction using the incompressible NS equations and the flexible plate dynamics. The NS equations (2) and (3) are solved by the lattice Boltzmann method (LBM).²⁷ The discrete lattice Boltzmann equation with the Bhatnagar-Gross-Krook (BGK) collision model is

$$f_i(\mathbf{x} + \mathbf{e}_i \Delta t, t + \Delta t) - f_i(\mathbf{x}, t) = -\frac{1}{\hat{\tau}} [f_i(\mathbf{x}, t) - f_i^{eq}(\mathbf{x}, t)] + \Delta t \mathcal{F}_i, \quad (5)$$

where f_i represents the distribution function for particles with velocity \mathbf{e}_i at position \mathbf{x} and time t . Δt is the time step. $\hat{\tau}$ is the non-dimensional relaxation time related to the fluid viscosity, $\nu = c_s^2(\hat{\tau} - 0.5)\Delta t$. f_i^{eq} is the equilibrium distribution function, which is defined as

$$f_i^{eq} = w_i \rho \left[1 + \frac{\mathbf{e}_i \cdot \mathbf{u}}{c_s^2} + \frac{(\mathbf{e}_i \cdot \mathbf{u})^2}{2c_s^4} - \frac{\mathbf{u}^2}{2c_s^2} \right], \quad (6)$$

and the force term \mathcal{F}_i is

$$\mathcal{F}_i = \left(1 - \frac{1}{2\hat{\tau}} \right) w_i \left[\frac{\mathbf{e}_i - \mathbf{u}}{c_s^2} + \frac{\mathbf{e}_i \cdot \mathbf{u}}{c_s^4} \mathbf{e}_i \right] \cdot \mathbf{f}, \quad (7)$$

where $c_s = c/\sqrt{3}$ is the speed of sound. $c = \Delta x / \Delta t$ is the lattice speed, where Δx is the grid spacing of the mesh. \mathbf{f} is the body force in Eq. (2). w_i is the weighting factor for the D2Q9 model,²⁸ where $w_i = 4/9$ for $i = 0$, $w_i = 1/9$ for $i = 1, 2, 3, 4$, $w_i = 1/36$ for $5, 6, 7, 8$. The D2Q9 model for 2D problem is

$$\mathbf{e}_i = c \begin{bmatrix} 0 & 1 & 0 & -1 & 0 & 1 & -1 & -1 & 1 \\ 0 & 0 & 1 & 0 & -1 & 1 & 1 & -1 & -1 \end{bmatrix}. \quad (8)$$

The plate dynamic equation (4) is solved by the nonlinear finite element method (FEM) with the large-displacement deformation

problem handled by co-rotational scheme.²⁹ The solvers LBM and FEM are coupled by the immersed boundary method.³⁰ The Lagrangian force \mathbf{F}_S can be calculated by the penalty scheme as

$$\mathbf{F}_S = \alpha \int_0^t [\mathbf{U}_f(s, t') - \mathbf{U}_s(s, t')] dt' + \beta [\mathbf{U}_f(s, t) - \mathbf{U}_s(s, t)], \quad (9)$$

where α and β are negative penalty parameters. t' is the time integral variable. \mathbf{U}_s is the Lagrangian velocity of the material point of the plate. \mathbf{U}_f is the fluid velocity at the position \mathbf{X} , which can be obtained by the following interpolation:

$$\mathbf{U}_f(s, t) = \int \mathbf{u}(\mathbf{x}, t) \delta(\mathbf{x} - \mathbf{X}(s, t)) dx. \quad (10)$$

Then the body force term in Eq. (2) is

$$\mathbf{f}(\mathbf{x}, t) = - \int \mathbf{F}_S(s, t) \delta(\mathbf{x} - \mathbf{X}(s, t)) ds. \quad (11)$$

The above numerical method has been widely utilized to solve fluid-structure interaction problems, such as flow over a flexible plate^{24,31} or an inverted flexible plate,³² self-propulsion or collective locomotion of flexible plates.³³⁻³⁶ The validation of the numerical method has been conducted in our previous works.^{25,35,37}

In our study, a typical case of a flapping flexible plate in a uniform incoming flow is simulated. The key non-dimensional parameters are $Re = 64$, $S = 1000$, $K = 8$, $M = 0.2$, and $\rho = 1$.

Regarding the study on computational domain independence, we conducted tests with different computational domains. The time step and grid spacing were kept constant at $\Delta t = 0.0001T$ and $\Delta x = 0.01L$, where $T = 1/f_c$ represents the flapping period. Figure 2 compares the evolution of the horizontal force F_x on the plate and the velocity (u, v) at the fixed point $(x, y) = (1, 0)$ in the wake. The results indicate almost no differences in hydrodynamic force and near-field velocity among cases with three different computational domains, suggesting that the domain $[-5, 10] \times [-5, 5]$ is sufficiently large to eliminate boundary effects. In this study, we selected $[-15, 45] \times [-15, 15]$ as the computational domain to obtain a long enough vortex wake for DMD analysis.

For the grid independence and the time step independence study, cases with $(\Delta x/L, \Delta t/T) = (0.02, 0.0002)$, $(\Delta x/L, \Delta t/T) = (0.01, 0.0001)$, and $(\Delta x/L, \Delta t/T) = (0.005, 0.00005)$ were tested. Figure 3(a) shows the horizontal force F_x on the flapping flexible plate as a function of time. Figure 3(b) show the velocity (u, v) at a fixed point $(x, y) = (1, 0)$ in the wake, which is the point closest to the trailing edge of the plate. It is seen that the force curves and velocity curves for $(\Delta x/L, \Delta t/T) = (0.01, 0.0001)$ and $(\Delta x/L, \Delta t/T) = (0.005, 0.00005)$ agree very well. On the other hand, the curves of $(\Delta x/L, \Delta t/T) = (0.02, 0.0002)$ has some discrepancies with those of $(\Delta x/L, \Delta t/T) = (0.01, 0.0001)$. Table I provides data for the horizontal force and velocity (u, v) at the point $(x, y) = (1, 0)$ at two specific time instances. The first data point corresponds to a time of $1.27T$ and represents the minimum value of the horizontal force. The second data point is at a time of $1.57T$ and corresponds to the maximum value of the horizontal force on the flapping flexible plate. The results of convergence studies show that $\Delta x/L = 0.01$ and $\Delta t/T = 0.0001$ are small enough to obtain accurate results.

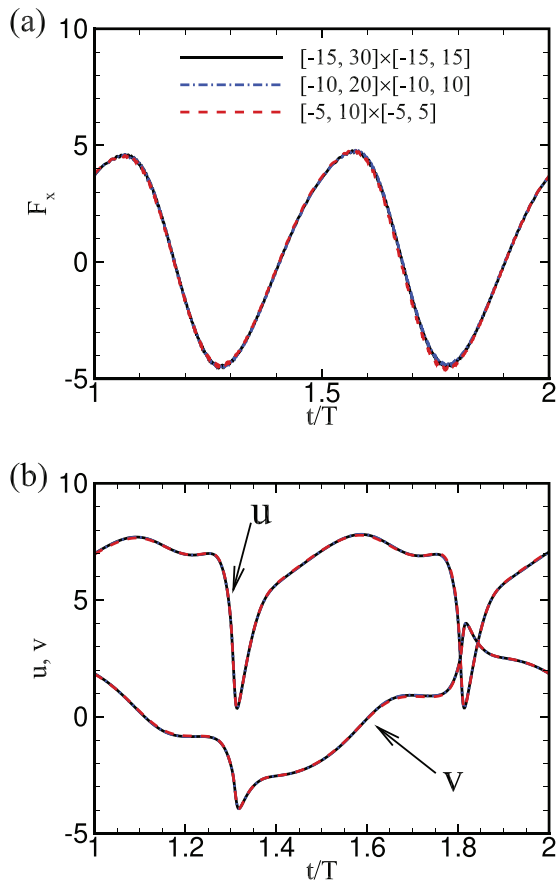


FIG. 2. The computational domain independence studies for the case of uniform incoming flow over a flapping flexible plate with the key non-dimensional parameters: $Re = 64$, $S = 1000$, $K = 8$, and $M = 0.2$. Panels (a) and (b) are the horizontal force F_x on the body and the velocity (u, v) at the mark point $(x, y) = (1, 0)$. F_x is scaled by $F_{ref} = 0.5\rho U_{ref}^2 L$. u and v are scaled by U_{ref} . The same force dimensionlessness applies to Figs. 3, 6(a), and 11–16.

C. DMD method

The basic idea behind DMD is to decompose a given dataset into a set of modes, each representing a distinct dynamic behavior with unique frequency. These modes capture the underlying dynamics of the system and provide a low-dimensional representation of the data.

We utilize DMD to process spatial-temporal data of fluids. The flow field in each snapshot is \hat{x}_k , which is made up of $n_x \times n_y$ grid points and flow variables of interest at every grid point. The dimensionless time interval between each snapshot is Δt^* , the number of snapshots used in DMD is N , the chosen snapshots are collected in two data matrices $\hat{X} = [\hat{x}_1, \hat{x}_2, \dots, \hat{x}_{N-1}]$ and $\hat{Y} = [\hat{x}_2, \hat{x}_3, \dots, \hat{x}_N]$. The first step of DMD assumes that the variables of the fluid satisfy an approximate linearization condition,

$$\hat{Y} = [\hat{x}_2, \hat{x}_3, \dots, \hat{x}_N] = [A\hat{x}_1, A\hat{x}_2, \dots, A\hat{x}_{N-1}] = A\hat{X}. \tag{12}$$

where A is the system matrix of the high-dimensional flow field, which is used to estimate the dynamic characteristics of the system. The goal of DMD is to extract dominant eigenvalues and primary modes by

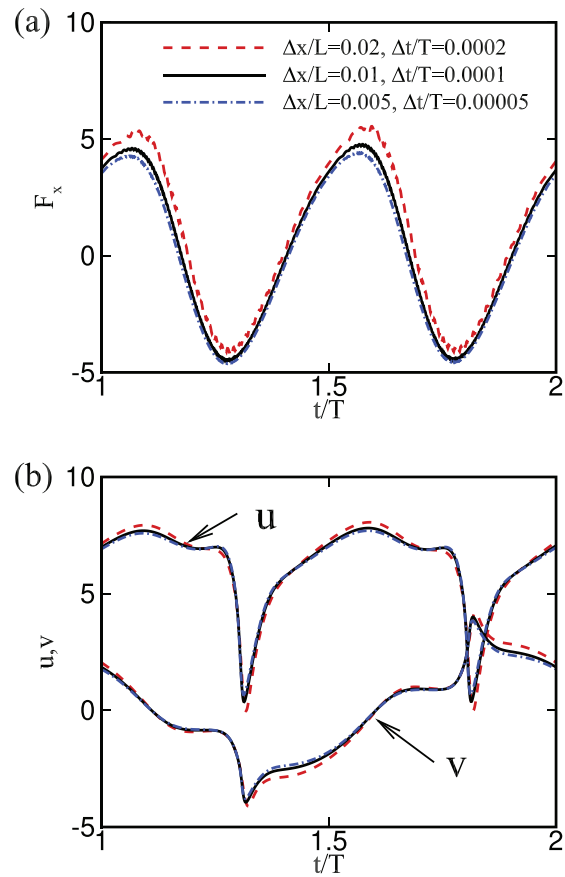


FIG. 3. The grid independence and time step independence studies for the case of uniform incoming flow over a flapping flexible plate with the key non-dimensional parameters: $Re = 64$, $S = 1000$, $K = 8$, and $M = 0.2$. Panels (a) and (b) are the horizontal force F_x on the body and the velocity (u, v) at $(x, y) = (1, 0)$.

applying mathematical transformations to the matrix A mentioned above.

Here, the DMD algorithm is briefly introduced as follow:

1. The matrix \hat{X} is decomposed with the singular value decomposition (SVD), namely, $\hat{X} = USV^T$.

TABLE I. The grid and time step independence study: The values of horizontal force and velocity at $(x, y) = (1, 0)$ at $t = 1.27T$ and $t = 1.57T$ for the flapping flexible plate model with key parameters, $Re = 64$, $M = 0.2$, $K = 8$, and $S = 1000$.

$\Delta x/L$	$\Delta t/T$	t/T	F_x	u	v
0.02	0.0002	1.27	-3.93	6.58	-1.00
0.01	0.0001	1.27	-4.42	6.83	-0.99
0.005	0.00005	1.27	-4.60	6.89	-0.99
0.02	0.0002	1.57	5.50	8.00	-0.79
0.01	0.0001	1.57	4.72	7.77	-0.70
0.005	0.00005	1.57	4.41	7.67	-0.67

27 October 2023 22:19:39

2. To efficiently compute matrix A , the first r columns of matrices U and V , and the first r rows and columns of matrix S are taken into consideration. Therefore, $\tilde{A} = U_r^T \tilde{Y} V_r S_r^{-1}$. The eigenvalues λ_j and eigenvector \tilde{v}_j of \tilde{A} can be obtained with the relationship of $\tilde{A} \tilde{v}_j = \lambda_j \tilde{v}_j$.
3. Each nonzero eigenvalue λ_i corresponds to a DMD mode Ψ_i as $\Psi_i = \mu_i^{-1} \tilde{Y} V_r S_r^{-1} \tilde{v}_i$.
4. The dimensionless frequency (f) of each DMD mode can be expressed as $f = \text{Im}(\log \lambda_i) / (2\pi \Delta t^*)$.
5. The instantaneous flow field can be approximately reconstructed by a linear combination of the DMD modes as $\hat{x}_t \approx \sum_{j=1}^r \Psi_j \lambda_j^{t-1} b_j$, where b_j denotes the amplitude of the DMD mode Ψ_j .

III. UNSTEADY FORCE EXPRESSION IN TERMS OF LOCAL VORTICAL STRUCTURES

“Vortices are the tendons of fluid motion.” The importance of studying vortex dynamics has been widely acknowledged and respected. Hence, vorticity has become a primary observational quantity in the description of nonlinear flow and the extraction of flow characteristics using the DMD method. Also, one of the central topics in vortex dynamics is to explore the relationship between vortex structures and the forces exerted on the body. The main objective of this section is to introduce the impulse theory for incompressible viscous flow and discuss the influence of different types of vorticity field on the forces acting on the body.

A typical external-flow problem is considered: a material body of volume V_B moves arbitrary in a viscous incompressible fluid, as shown in Fig. 4. To be sufficiently general, we permit bodies having arbitrary deformable boundary as in cases of fish swimming and insect flight in external biofluid dynamics, of nonlinear fluid-solid coupling, and of flow control by flexible walls, etc. By Newton’s third law the total force exerted to the body by the fluid is expressed as

$$F(t) = - \int_{\partial B} (-pn + \tau) dS, \tag{13}$$

where p is the pressure, $\tau = \mu \omega \times n$ is the viscous force, ∂B is the surface of the body domain V_B . n is the normal vector on the body surface. This force formula serves as a standard result for force calculation, the primary form of which distinguishes the normal and tangent components of the stress. However, it keeps silence on what

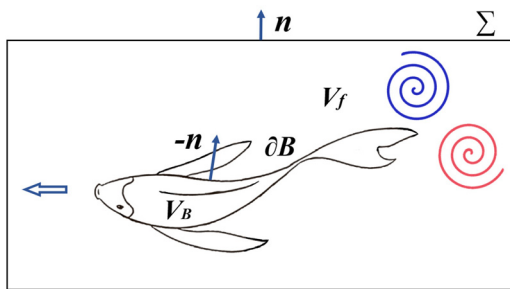


FIG. 4. Schematic illustration of a material body of volume V_B moving arbitrary in a viscous fluid. ∂B is the body surface. The analysis flow field, V_f , is bounded internally by the material surface ∂B and externally by a boundary Σ . n is the unit normal vector pointing outside of V_f .

flow structures generated by the body motion are major causes of the force, despite huge amount of flow visualization results obtained either experimentally or numerically have revealed the crucial importance of these structures for the total force. Equation (13) can be rewritten by integrals of local momentum balance in a generic control domain V_f

$$F = - \int_{V_f} \rho a dV + \int_{\Sigma} (-pn + \tau) dS. \tag{14}$$

Using the derivative moment transformations,¹⁶ we can relate the hydrodynamic force on the solid body V_B to the local vorticities by the finite-domain impulse theory,¹⁷

$$F = F_I + F_L + F_{\partial B} + F_{\Sigma}, \tag{15}$$

where

$$F_I = - \frac{dI_f}{dt} - F_{I\Sigma}, \quad I_f = \frac{1}{n-1} \int_{V_f} \mathbf{x} \times \rho \omega dV, \tag{16}$$

$$F_{I\Sigma} = \frac{1}{n-1} \int_{\Sigma} \mathbf{x} \times \rho \omega (\mathbf{u} - \mathbf{v}) \cdot \mathbf{n} dS, \tag{17}$$

$$F_L = - \int_{V_f} \rho \omega \times \mathbf{u} dV, \tag{18}$$

$$F_{\partial B} = \frac{1}{n-1} \int_{\partial B} \mathbf{x} \times (\mathbf{n} \times \rho \mathbf{a}) dS + \frac{1}{n-1} \int_{\partial B} \mathbf{x} \times \rho \omega \omega_n dS, \tag{19}$$

$$F_{\Sigma} = \frac{1}{n-1} \int_{\Sigma} \mathbf{x} \times \rho \omega \omega_n dS + \frac{1}{n-1} \int_{\Sigma} (\mathbf{x} \times \rho \boldsymbol{\sigma} + \boldsymbol{\tau}) dS. \tag{20}$$

Here V_f is arbitrary fluid domain surrounding the body, which has an arbitrary external boundary Σ . The velocity of the boundary is denoted by \mathbf{v} . n is the dimension degree of space. d is the derivative operator. $\mathbf{a} = D\mathbf{u}/Dt$ is the acceleration of the fluid, where D is the material derivative. $\boldsymbol{\sigma} = \mu \partial \omega / \partial n$ is the vorticity diffusive flux. I_f represents the vortical impulse. $F_{I\Sigma}$ is the force induced by the impulse overflow at the boundary Σ . So if the outer boundary Σ is a material boundary with $\mathbf{v} = \mathbf{u}$, then $F_{I\Sigma}$ is zero. If the outer boundary Σ is a fixed domain, $\mathbf{v} = \mathbf{0}$. F_I is the vortex force,¹⁶ which is the integral of Lamb vector in fluid domain. $F_{\partial B}$ represents the explicit effect of body motion and deformation, which is a prescribed integral for active motion/deformation and independent of the flow field. $\omega_n = \boldsymbol{\omega} \cdot \mathbf{n}$. F_{Σ} represents the hydrodynamic force caused by vorticity on outer boundary Σ .

The model in our numerical simulation is a two-dimensional incompressible flow around a plate without thickness, and for simplicity, the density of fluid ρ is assumed to be 1. In addition, to be consistent with DMD decomposition based on Euler field, we set the outer boundary of the analysis domain Σ to be fixed with $\mathbf{v} = \mathbf{0}$. For the plate without thickness, due to the adherence of \mathbf{a} , \mathbf{u} , and ω_n , $F_{\partial B} = 0$. F_{Σ} contains two terms: one is the viscous effect and can be ignored at large Reynolds number, and the other is due to the cutting of vorticity field at the outer boundary Σ , which is zero for two dimensional flow. So the hydrodynamic force Eq. (15) on the plate can be reduced to

$$F = F_I + F_L + F_{\Sigma}, \tag{21}$$

where

$$F_I = - \frac{d}{dt} \int_{V_f} \mathbf{x} \times \omega dV - \int_{\Sigma} \mathbf{x} \times \omega \omega_n dS, \tag{22}$$

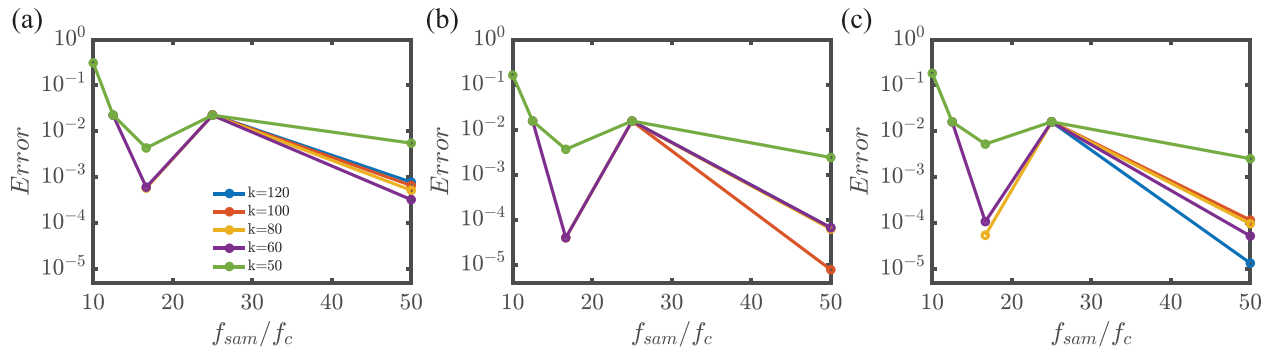


FIG. 5. Error trends of mode characteristic value for mode (a) $f^* = 0$, (b) $f^* = 1$, and (c) $f^* = 2$, where $f^* = f/f_c$, f_c is the flapping frequency, f is the characteristic frequency. Here f_{sam} is the sampling frequency. k is the sample number. The reference case is $f_{sam}/f_c = 50$, $k = 250$. The errors are calculated by $Error = |\lambda_i - \lambda_{i,ref}|/|\lambda_{i,ref}|$, where λ_i is the eigenvalue of i -th mode.

$$F_L = - \int_{V_f} \boldsymbol{\omega} \times \mathbf{u} dV, \tag{23}$$

$$F_\Sigma = \int_\Sigma (\mathbf{x} \times \boldsymbol{\sigma} + \boldsymbol{\tau}) dS. \tag{24}$$

It is seen that each term of Eq. (21) is a linear function of vorticity. Hence, whether the vorticity field is decomposed in space or function form, the corresponding force expression can also achieve the corresponding decomposition. Corresponding to DMD analysis method, we discuss the decomposition of vorticity field in function form. If $\boldsymbol{\omega}$ can be decomposed into the following form, i.e.,

$$\boldsymbol{\omega}(\mathbf{x}, t) = \sum_i \boldsymbol{\omega}_i(\mathbf{x}, t), \tag{25}$$

then

$$F(t) = \sum_i F_i(t), \quad F_i(t) = F_{L,i} + F_{L,i} + F_{\Sigma,i}, \tag{26}$$

where

$$F_{L,i} = - \frac{d}{dt} \int_{V_f} \mathbf{x} \times \boldsymbol{\omega}_i dV - \int_\Sigma \mathbf{x} \times \boldsymbol{\omega}_i u_n dS, \tag{27}$$

$$F_{L,i} = - \int_{V_f} \boldsymbol{\omega}_i \times \mathbf{u} dV, \tag{28}$$

$$F_{\Sigma,i} = \int_\Sigma \left(\mathbf{x} \times \mu \frac{\partial \boldsymbol{\omega}_i}{\partial n} + \mu \boldsymbol{\omega}_i \times \mathbf{n} \right) dS. \tag{29}$$

Using these formulas, we can obtain the contribution of each DMD mode to the force, and find out the key modes and influencing mechanisms that affect the force on the body.

IV. RESULTS AND DISCUSSION

A. Convergence study to select DMD modes and sampling frequency

The process to determine the number of DMD samples and the sampling frequency is briefly presented. The numerical simulation is run at $\Delta t = 0.0001T = 0.0001/f_c$ time steps. Here, we utilize the DMD decomposition statistics obtained from 250 samples at frequency $f_{sam} = 50f_c$. A convergence study of the number of DMD

samples and the sampling frequency is carried out. Figure 5 shows the error of mode energy of three most energetic modes in comparison with reference sampling. We chose a series of sampling frequency and number of snapshot to validate the accuracy of DMD. The relative error (RE) is below 1.5% once the dimensionless sampling frequency exceeds 12.5. As sampling frequency and snapshot number increase, the RE decreases.

B. DMD for vortical flow over a plate

In this section, the DMD method is employed to extract the spatial-temporal characteristics of the flow field around a flapping flexible plate. Figure 6(a) shows the temporal domain for the DMD analysis, where the snapshots for DMD analysis are generated over the range $t/T \in [10, 15]$ with the time interval of $\Delta t_{sam}/T = 0.02$ ($T = 1/f_c$ denotes the flapping period). As shown in Fig. 6(b), the snapshots are extracted from $[-2, 30] \times [-5, 5]$, which contains about five pairs of vortices. Note that the DMD analysis is performed when the time-averaged performance metrics change by less than 1%.

Figure 7(a) presents the eigenvalue distribution of DMD modes in the complex space and the amplitude of DMD modes is shown in Fig. 7(b). It is evident from Fig. 7(b) that the frequencies of the dominant DMD modes are all integral multiples of the plate's flapping

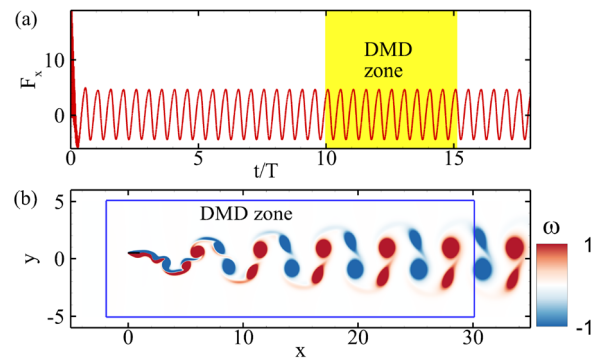


FIG. 6. (a) The sampling time domain and (b) the sampling spatial domain of the DMD process. The yellow zone in Panel (a) covers the time range $t/T \sim [10, 15]$. The region inside the blue box satisfies $(x, y) \in [-2, 30] \times [-5, 5]$.

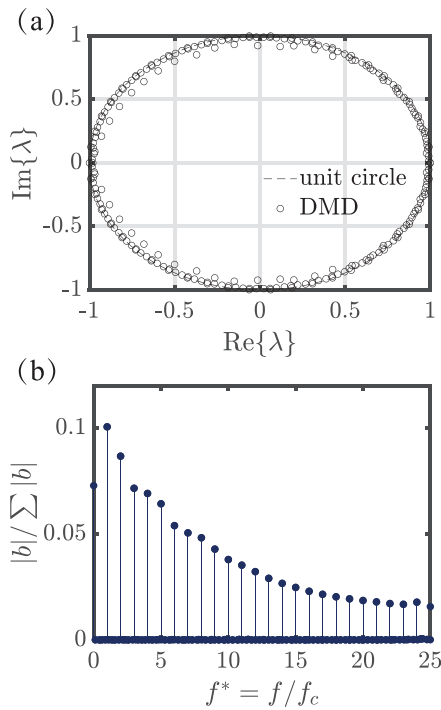


FIG. 7. (a) Eigenvalue distribution of DMD modes. (b) Energy amplitude distribution of DMD modes as a function of dimensionless frequency. The snapshot number $k = 250$ and dimensionless sampling frequency $f_{\text{sam}}/f_c = 50$ here.

frequency f_c . Figure 8 shows the vorticity contours for modes 1 to 8, where mode 1 ($f^* = 0$) denotes the time-averaged vorticity field. Mode 2 ($f^* = 1$) represents the primary vortex street, which is consistent with the 2P wake vortex street in the original flow field. Another noteworthy point is that modes 2, 4, 6, and 8 ($f^* = 1, 3, 5, 7$) show symmetric vortical wake patterns, corresponding to the convection of large scale structures downstream the plate.³⁸ Modes 1, 3, 5, and 7 ($f^* = 0, 2, 4, 6$) show anti-symmetric wake patterns, corresponding to the shedding of the vortices in the wake of the plate.

To quantitatively verify the feasibility of the DMD modes, the flow fields reconstructed by the DMD modes are compared with the original flow field shown in Fig. 9. It can be seen that the error between the flow field reconstructed by the first 25 modes and the original flow field is only 0.12%, which demonstrates the correctness of the DMD results. It also implies that the DMD modes with high amplitude are the dominant components of the original flow field.

Here, we use enstrophy $\omega^2/2$ to estimate the total amount of shearing in the flow domain for each mode. As is shown in Fig. 10(a), we measured the enstrophy integral on each x-cross section in the wake of the plate, i.e., $\int_{x_W} \omega^2/2 dS$, where x_W is the x-coordination of the integral surface. It can be seen that, except for the first few modes, enstrophy decreases significantly as the wake integral cross section moves downstream. With the increase in mode number, the enstrophy decreases obviously. Figure 10(b) shows the integral of the enstrophy on the whole DMD spatial domain and the wake vortical region ($x \geq 2$) for each mode, respectively. We found that, except for mode 1, the enstrophy of the entire DMD zone and the wake region ($x \geq 2$) decreases significantly with the increase in the modes. The variation trend of enstrophy with DMD modes is consistent with that of energy

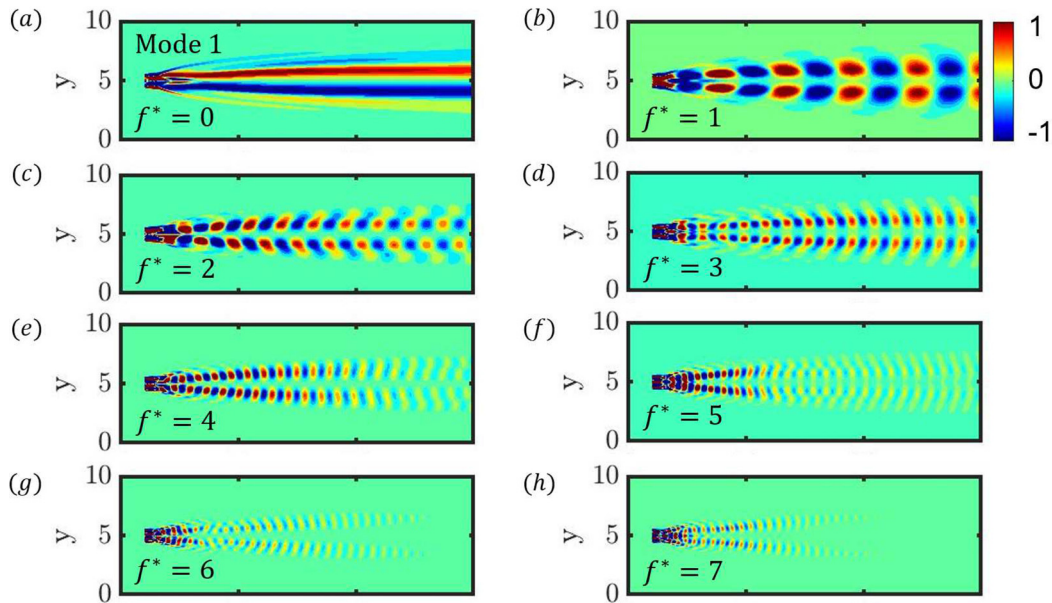


FIG. 8. DMD of flow around a flapping flexible plate. Panels (a)–(h) are corresponding to modes 1–8. The vorticity ranges from -1 (blue) to 1 (red). The vorticity is non-dimensionalized by U_{ref}/L .

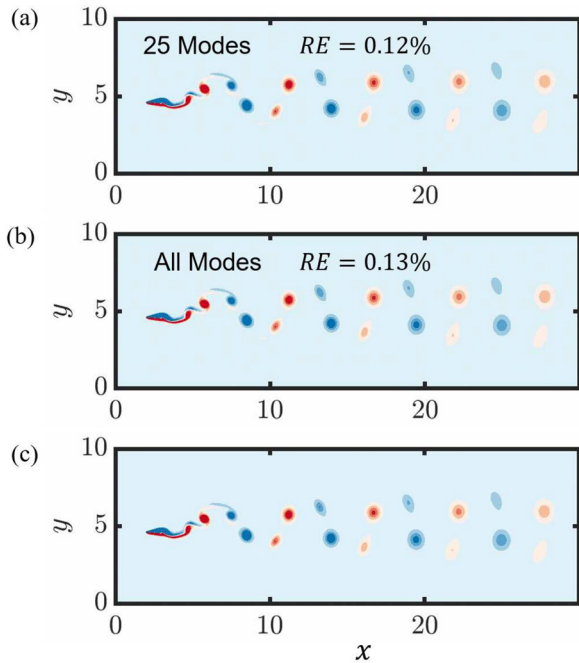


FIG. 9. Reconstruction of the time series vorticity field using different number of modes. (a) 25 modes. (b) all modes. (c) original vorticity field. The RE is defined as $RE = \sum_{m=1}^{250} |\hat{X}_{nm,m} - \hat{X}_m| / |\hat{X}_m|$, where m is the sequence number of snapshot, n_M is the number of the modes, \hat{X} is reconstructed vorticity field and \hat{X} is original vorticity field. The vorticity ranges from -10 (blue) to 10 (red). The vorticity is non-dimensionalized by U_{ref}/L .

amplitude with DMD modes in Fig. 7(b). Especially for the case of mode ≥ 10 , the vorticity in the wake region can be basically ignored. Considering the impulse theory mentioned before, only the domain with vorticity contributes to the force. It can be inferred that the contributions of the high frequency modes to the force does not depend on the selection of the wake region.

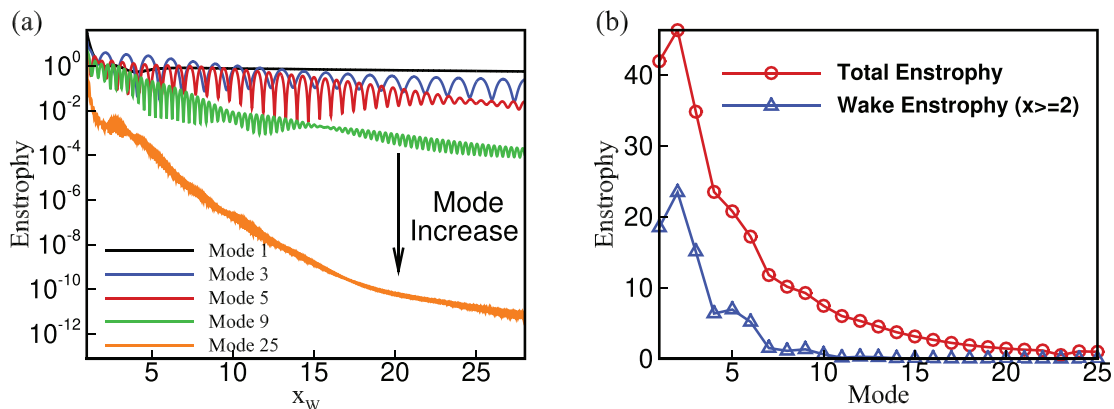


FIG. 10. (a) The enstrophy integral on each x -cross section in the wake of the plate as a function of the x -coordinate of the x -cross section, x_w . (b) The enstrophy integral in the fluid domain contributed by each mode.

C. Force contribution by DMD modes

From the observation of Fig. 6(b), it can be concluded that the reversed Kármán vortex street generates two vortices with the same sign within half a cycle, and its flow can be classified as the 2P wake mode.³⁹ Furthermore, through the DMD analysis discussed in Sec. IV B, it is evident that the vortical structures of each mode significantly differ from those of the actual flow field. In this section, we utilize the expression (26) to analyze the force contributions of DMD modes for the flapping flexible plate.

Figure 11(a) depicts the time-varying force, where F_x and F_y represent the horizontal and lateral components of the total hydrodynamic force acting on the plate. We utilized Eq. (21) on the real vorticity field to estimate the force exerted on the plate. We then compared this approximation with the conventional outcome obtained from Eq. (13). Our investigation reveals that the force data can be effectively obtained through the utilization of the real vorticity field. To capture the primary modes that contribute to the force, we calculate the cumulative contribution of the first n_M modes. We observe that the cumulative contribution of the initial 8 modes encompasses the majority of the force information. Furthermore, when considering $n_M = 15$, the reconstruction of the force achieves a satisfactory level of accuracy.

Figure 12 also presents the mean absolute error (MAE) and relative error (RE) associated with the force computation using the cumulative sum of the first n_M modes. The MAE and RE are calculated using the following equations:

$$MAE(n_M) = \frac{1}{50} \sum_{m=1}^{50} |\hat{F}_{n_M,m} - F_{STD,m}|, \quad (30)$$

$$RE(n_M) = \frac{1}{50} \sum_{m=1}^{50} |\hat{F}_{n_M,m} - F_{STD,m}| / |F_{STD,m}|. \quad (31)$$

Here, n_M represents the number of modes to be summed, m denotes the snapshot's sequence number, $\hat{F}_{n_M,m}$ signifies the force at $t/T = 10 + (m - 1)/50$ computed using the cumulative sum of the first n_M modes, i.e., $\hat{F}_{n_M} = F_1 + F_2 + \dots + F_{n_M}$, where F_i is the force contributed by i th mode calculated by Eq. (26). $F_{STD,m}$ denotes the standard result obtained from Eq. (13). Additionally, we computed the MAE and RE for the force calculated using the actual vorticity field. Although the enstrophy of the DMD flow field does not converge for

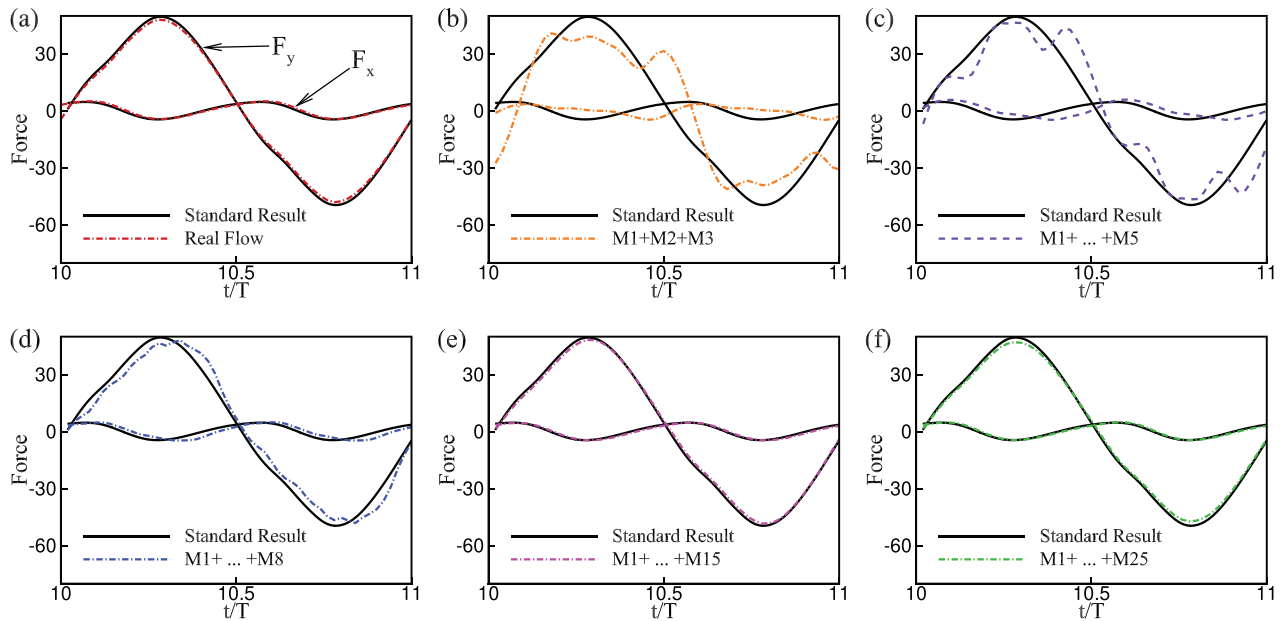


FIG. 11. The evolution of the force on the flapping flexible plate: The standard result is calculated by Eq. (13). The forces contributed by (a) the real flow and the sum of the first n_M modes [(b) $n_M=3$, (c) $n_M=5$, (d) $n_M=8$, (e) $n_M=15$, and (f) $n_M=25$] are calculated by Eqs. (21) and (26), respectively.

$n_M = 15$, it is evident that when $n_M \geq 15$, the force is accurately calculated with a high degree of accuracy, approaching that of the real flow. This suggests that the number of essential modes associated with the force is smaller than the number required for the evolution of the flow field.

As explained in Sec. III, the hydrodynamic force exerted on the body is determined by integrating a function of vorticity over the fluid domain V_f and its outer boundary Σ . Therefore, the choice of the fluid

domain can impact the accuracy of predictions using the first fifteen modes, which demonstrate good results when the x-coordinate of the wake surface of Σ , x_w , is set to 30. Figure 10 also illustrates the rapid decay of the vorticity wake as the mode number increases. Furthermore, Fig. 13 provides additional insight into the influence of the integration domain on the accuracy of force calculations using the first fifteen modes. The standard result is obtained using Eq. (13). Notably, the force components (F_x , F_y) calculated using Eq. (26) with different analysis domains exhibit close agreement with the standard surface stress integral. This confirms that the results are independent of the size of the wake domain, at least for $x_w \geq 3$.

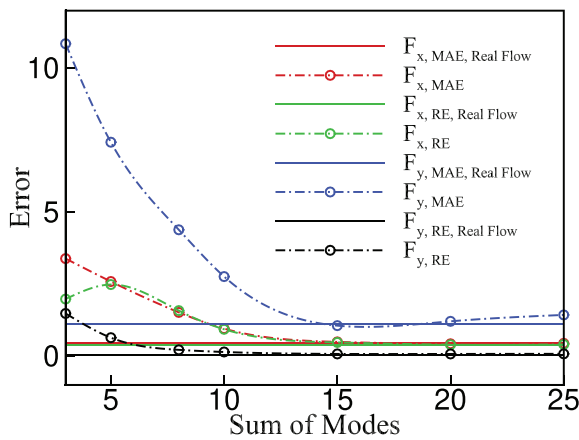


FIG. 12. The error of the force prediction by the sum of the first n_M modes as a function of n_M . $F_{x,MAE,RealFlow}$ and $F_{x,RE,RealFlow}$ represent the MAE calculated by Eqs. (30) and (31) for the horizontal force prediction of real flow respectively. $F_{x,MAE}$ and $F_{x,RE}$ represent the MAE calculated by Eqs. (30) and (31) for the horizontal force prediction of the sum of the first n_M modes, respectively. The subscript y indicates the corresponding lateral force prediction.

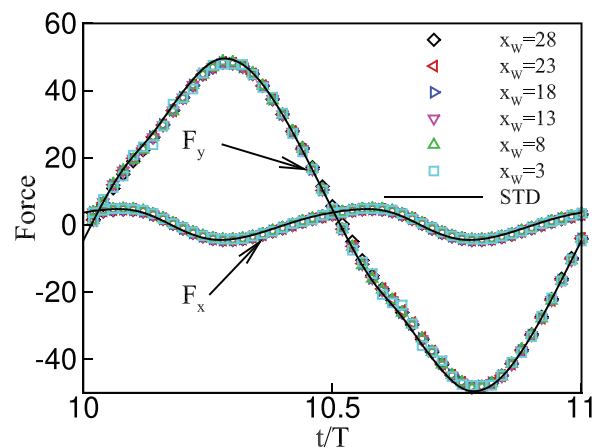


FIG. 13. The influence of integral domain on the accuracy of the force calculation contributed by the first fifteen modes. The x-coordinate of the wake surface of Σ is represented by x_w . STD is the standard result calculated by Eq. (13).

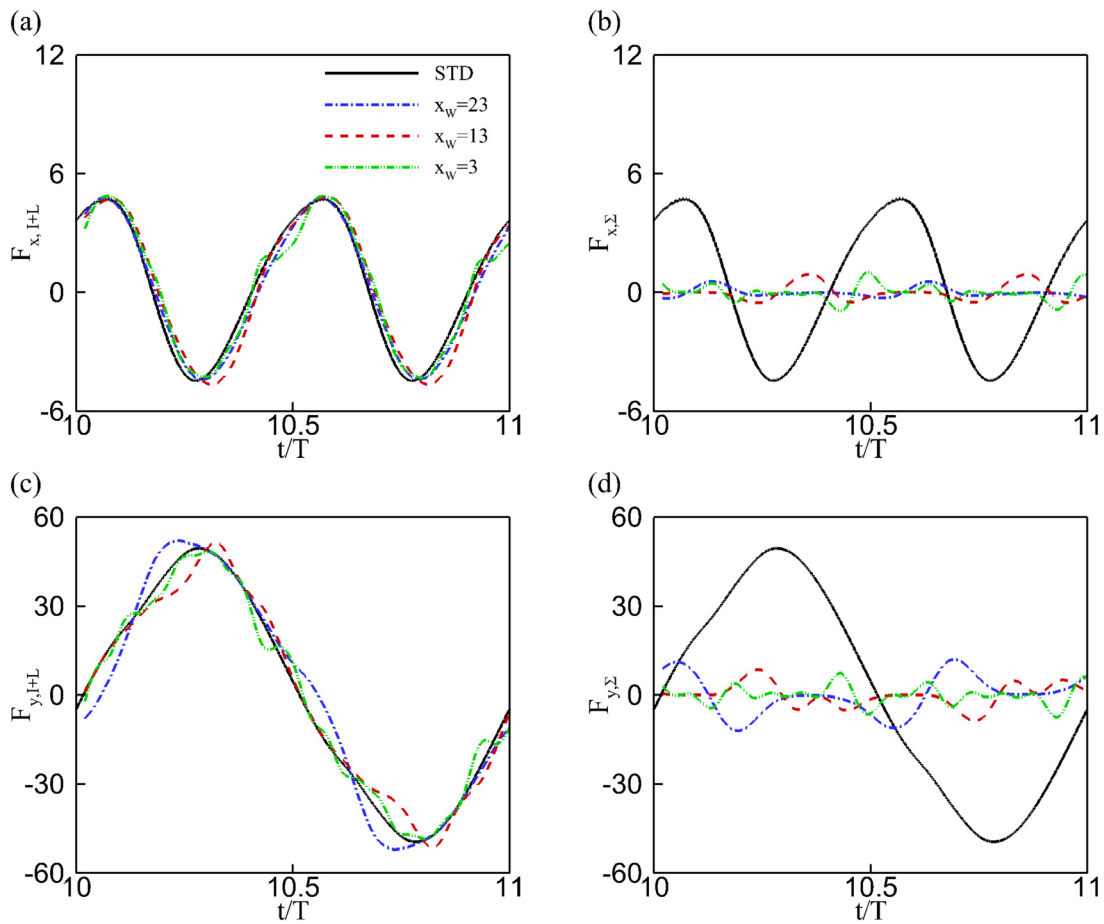


FIG. 14. Time evolutions of (a) and (b) horizontal component and lateral component (c) and (d) of the force contributed by (a) and (c) the impulse force and vortex force and (b) and (d) the Σ -force for the first fifteen modes. STD is the standard result calculated by Eq. (13). x_w is the x-coordinate of the wake surface of the outer boundary Σ .

In order to further investigate the impact of the choice of integral domain on different force components, Fig. 14 illustrates the temporal evolution of the force contributed by the cumulative sum of the impulse force and vortex force [F_I and F_L in Eq. (21)], as well as the

Σ -force [F_Σ in Eq. (21)] of the first fifteen modes for various integral domains. The results reveal that the force is primarily influenced by the cumulative sum of the impulse force and vortex force. Importantly, the conclusion remains largely unaffected by the selection of the wake’s integral cross section.

Furthermore, we examined the individual force contributions from each mode and discovered that the primary contributions stem from the initial modes. It can also be seen from Fig. 11(d) that the force curve $\hat{F}_8 (= F_1 + F_2 + \dots + F_8)$ is very close to that of standard result, which means that the force amplitude of the modes greater than 8 is already small. Figure 15 illustrates the force contributed by the first five modes. As depicted in Fig. 15(a), the hydrodynamic force induced by the first mode with $f^* = 0$ corresponds to a thrust, providing strong evidence for the thrust associated with the wake’s mean flow field in a jet pattern [Fig. 8(a)]. The results also demonstrate that mode 2 with $f^* = 1$ contributes to a drag force. In addition, Fig. 15(b) reveals that the lateral force is predominantly influenced by mode 2, which exhibits the most pronounced antisymmetric vortex street.

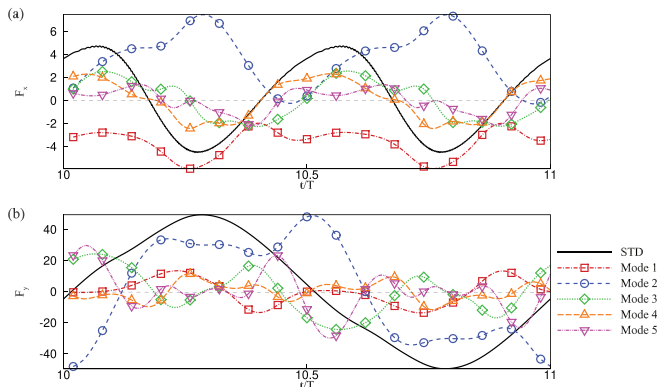


FIG. 15. (a) The horizontal force F_x and (b) the lateral force F_y contributed by each mode (mode = 1, 2, 3, 4, 5) as a function of time. STD is calculated by Eq. (13).

Figure 16 presents the time-averaged horizontal force \bar{F}_x and lateral force \bar{F}_y as a function of modes with different frequencies. To calculate the time-averaged values, we can use Eqs. (27)–(29). The

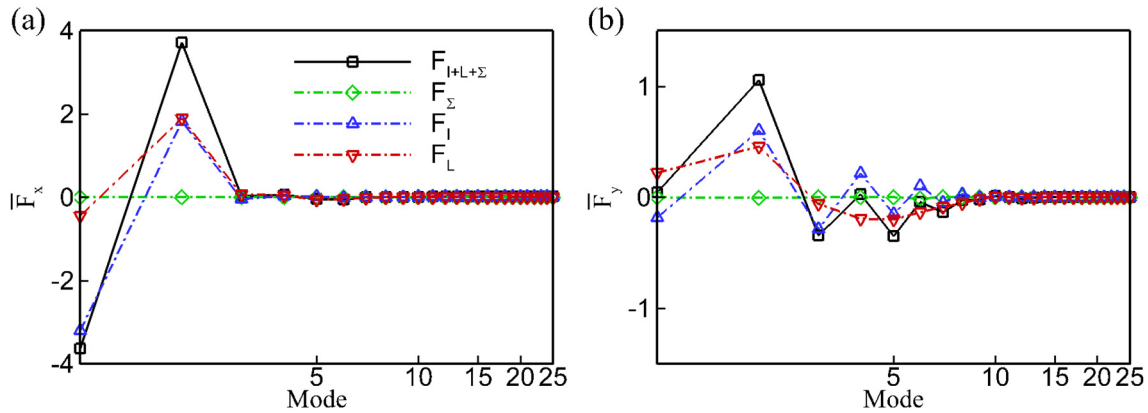


FIG. 16. Time-averaged (a) horizontal force \bar{F}_x and lateral force \bar{F}_y contributed by each force term calculated by doing time average of Eq. (26) for each mode. F_I , F_L and F_Σ are calculated by Eqs. (27)–(29). $F_{I+L+\Sigma} = F_I + F_L + F_\Sigma$.

expressions for the time-averaged impulse force $\bar{F}_{I,i}$, vortex force $\bar{F}_{L,i}$, and force $\bar{F}_{\Sigma,i}$ are as follows:

$$\bar{F}_{I,i} = \int_{x=x_W} \overline{\mathbf{x} \times \omega_i \mathbf{u}} dS \approx U_\infty \int_{x=x_W} \overline{\mathbf{x} \times \omega_i} dS, \quad (32)$$

$$\bar{F}_{L,i} = \int_{V_j} \overline{\omega_i \times \mathbf{u}'} dV, \quad (33)$$

$$\bar{F}_{\Sigma,i} = \mathbf{0}. \quad (34)$$

Here, $\mathbf{u}' = \mathbf{u} - U_\infty \mathbf{e}_x$ represents the disturbance velocity, which accounts for the difference between the actual velocity \mathbf{u} and the free-stream velocity U_∞ .

The results in Fig. 16 indicate that the horizontal force is primarily contributed by the first two modes, specifically mode 1 with $f^* = 0$ and mode 2 with $f^* = 1$. The net thrust contributed by mode 1 is mainly attributed to the impulse force F_I , while the net drag contributed by mode 2 is a combination of the impulse force F_I and the vortex force F_L . On the other hand, the lateral force is mainly influenced by modes 2, 3, and 5. mode 2 with $f^* = 1$ contributes to a positive lateral force, while modes 3 and 5 with $f^* = 2$ and $f^* = 4$, respectively, contribute to a negative lateral force. Notably, the lateral force contributed by the impulse force oscillates as the mode increases. Additionally, F_Σ does not contribute to the time-averaged force. Referring to Fig. 17, it can be observed that, except for mode 1, the vorticity of each mode at a fixed point varies sinusoidally with a zero time-averaged value. So there is no net F_Σ in time average sense.

V. CONCLUSION

Despite the prevalence of DMD analysis, there are very few studies on its application to an accurate understanding of the force development process of fluid-structure interaction problems. In this paper, we considered the flexible plate flapping in a uniform incoming flow. We utilized DMD decomposition and impulse theory to interpret the most significant vortical wake features and their contributions to the force on the flexible plate interacting with incoming flow. Three distinct features of the DMD modes of the organized motion are identified, namely, the shear layer (mean flow field $f^* = 0$), wake composed

of two symmetrical vortex streets (f^* is even number), wake composed of two antisymmetrical vortex streets (f^* is odd number). We observed that the twenty five most energetic modes (mode 1 to mode 25) contain $\approx 99.8\%$ of the energy. We used the enstrophy to detect the wake vortex strength of each mode and found that after a body length downstream of the plate the enstrophy is basically contributed by the first ten modes.

By impulse theory, we found that the force of the plate is strongly dominated by the several most energetic modes. The integrated force contribution of the first fifteen modes is close to the standard result of the surface stress integral, which does not depend on the selection of the wake integral region. Further, we identify that the net horizontal force is mainly contributed by the shear flow ($f^* = 0$) and the first vortex shedding mode ($f^* = 1$), where the former contributes thrust and the later contributes drag. The net lateral force is mainly contributed by the modes with $f^* = 1, 2, 4$, where the first mode contributes the force in the opposite direction to the last two.

In this work, the intrinsic relationship between the physical field analyzed by DMD method and the force on the body is discussed from the perspective of vorticity dynamic theory for the first time, and it is applied to the analysis of fluid-structure interaction problem. By identifying the key modes that affect the force of the body, it will be beneficial to realize the control of the dynamic system in a targeted way. Although the current analysis strategy is only applied to the flapping plate case, it is universal and will help to deepen our understanding of the physical mechanism and select key physical information for flow control.

It is worth noting that we have not explored scenarios with high Reynolds numbers. In such cases, the nonlinear effects within the system become more pronounced, presenting new challenges for the application of the DMD method, which is based on the assumption of linear approximations. This underscores the necessity for further research in the future regarding the use of DMD to predict high Reynolds number turbulence.

Furthermore, this paper exclusively focuses on DMD theory related to spatiotemporal data decomposition and does not explore other decomposition theories such as proper orthogonal decomposition (POD). We would like to emphasize that conducting a

comprehensive comparative study of various dimensionality reduction models could strengthen the conclusions of this paper.

ACKNOWLEDGMENTS

The authors acknowledge the support of the National Natural Science Foundation of China (Grant No. 12102365), National Key Research and Development Program of China (Grant No. 2022YFC2805200), and the Startup funding of New-joined PI of Westlake University with Grant No. 041030150118.

AUTHOR DECLARATIONS

Conflict of Interest

The authors have no conflicts to disclose.

Author Contributions

Linlin Kang: Conceptualization (equal); Data curation (equal); Formal analysis (equal); Funding acquisition (equal); Investigation (equal); Methodology (equal); Project administration (equal); Resources (equal); Software (equal); Validation (equal); Visualization (equal); Writing – original draft (equal); Writing – review & editing (equal). **Shiyong Xiong:** Conceptualization (equal); Formal analysis (equal); Project administration (equal); Supervision (equal); Writing – original draft (equal); Writing – review & editing (equal). **Buchen Wu:** Conceptualization (equal); Formal analysis (equal); Project administration (equal); Supervision (equal); Writing – original draft (equal); Writing – review & editing (equal). **Chao Li:** Data curation (equal); Software (equal); Validation (equal); Visualization (equal); Writing – original draft (equal). **Mingming Ge:** Writing – original draft (equal). **Dehan Yuan:** Writing – original draft (equal). **Fei Han:** Writing – original draft (equal). **Weicheng Cui:** Writing – original draft (equal); Writing – review & editing (equal).

DATA AVAILABILITY

The data that support the findings of this study are available from the corresponding authors upon reasonable request.

NOMENCLATURE

Physical model and mathematical formulation

a	Acceleration of the fluid
A	Flapping amplitude
e_x	Unit vector in x direction
Eh	Structural stretching rigidity
EI	Structural bending rigidity
f	Eulerian force vector
f_c	Flapping frequency
F_S	Lagrangian force vector
K	Bending stiffness ($K = EI/\rho U_{ref}^2 L^3$)
L	Length of the plate
M	Mass ratio of the plate ($M = \rho_s h/\rho L$)
p	Pressure of the fluid
Re	Reynolds number ($Re = \rho U_{ref} L/\mu$)
s	Lagrangian coordinate along the plate

S	Stretching stiffness ($S = Eh/\rho U_{ref}^2 L$)
t	time
u	Velocity vector, $u = (u, v)$
u'	Disturbance velocity
U_∞	Uniform incoming fluid flowing velocity
U_{ref}	Reference velocity for nondimensionalization ($U_{ref} = Lf_c$)
x	position vector for flow fluid, $x = (x, y)$
x_L	coordinate of the leading edge of the plate
y_L	Coordinate of the leading edge of the plate
X	Position vector for plate
μ	Dynamic viscosity of fluid
ν	Kinematic viscosity of fluid
σ	Vorticity diffusive flux
ρ	Density of the fluid
$\rho_s h$	Structural linear mass density

Numerical method for simulation

c	Lattice speed
c_s	Speed of sound
e_i	Velocity of particle
f_i	Distribution function for particles
f_i^{eq}	Equilibrium distribution function for particles
\mathcal{F}_i	External force corresponding to body force f
T	Flapping period, $T = 1/f_c$
U_f	Fluid velocity at position X
U_s	Lagrangian velocity of material point of plate
w_i	Weighting factor for D2Q9 model
α, β	Penalty parameters
Δt	Time step
Δx	Spatial step
$\hat{\tau}$	Non-dimensional relaxation time

Force analysis

d/dt	Time derivative of the integration variable
D/Dt	Material derivative in a continuous medium
F	Total hydrodynamic force on plate, $F = (F_x, F_y)$
F_x	x-Component of hydrodynamic force on plate
F_y	y-Component of hydrodynamic force on plate
F_I	Impulse force
$F_{I\Sigma}$	Force induced by impulse overflow at boundary Σ
$F_{\partial B}$	Force corresponding to body motion and deformation
F_Σ	Force caused by vorticity on boundary Σ
\bar{F}_x	Time-averaged horizontal force
\bar{F}_y	Time-averaged lateral force
I_f	Vortical impulse
k	Sample number of DMD
n	Dimension of space
\mathbf{n}	Normal vector on the surface pointing outside of V_f
V_B	Body domain
V_f	Fluid domain
x_W	x-Coordinate of the wake integral surface
τ	Viscous force, $\tau = \mu\omega \times \mathbf{n}$
v	Velocity of boundary Σ
Σ	External boundary of fluid domain
σ	Vorticity diffusive flux
$\partial/\partial t$	Time partial derivative of continuous fields

- ∂B surface of body domain V_B
- $\boldsymbol{\omega}$ Vorticity
- $\boldsymbol{\omega}_i$ Vorticity of i th DMD mode

DMD analysis

- \mathbf{A} System matrix in DMD
- b_i Amplitude of DMD mode
- f Characteristic frequency of DMD mode
- f_{sam} Frequency of DMD samples, $f_{\text{sam}} = 50f_c$
- f^* Non-dimensional characteristic frequency of DMD mode
- \mathbf{F} Contributed by i th mode
- \mathbf{F}_i Hydrodynamic force
- $\mathbf{F}_{l,i}$ \mathbf{F}_l Contributed by i th DMD mode
- $\mathbf{F}_{L,i}$ \mathbf{F}_L Contributed by i th DMD mode
- $\mathbf{F}_{\Sigma,i}$ \mathbf{F}_{Σ} Contributed by i th DMD mode
- $\hat{\mathbf{F}}_{n_M}$ Summed force contribution of the first n_M modes
- MAE Mean absolute error of force prediction
- n_M Number of modes to be summed
- RE Relative error of force prediction
- $\hat{\mathbf{x}}_k$ Flow field in each snapshot
- $\hat{\mathbf{X}}, \hat{\mathbf{Y}}$ Date matrices of snapshots
- Δt_{sam} Time interval of DMD samples
- λ Eigenvalue of i th DMD mode

APPENDIX A: DERIVATION DETAILS OF IMPULSE THEORY

1. Derivative Moment Transformation

For any piecewise differentiable vector field \mathbf{g} and scalar field ζ in n -dimensional space with $n = 2, 3$, there are two vectorial integral identities

$$\int_V \mathbf{g} = \frac{1}{n-1} \int_V \mathbf{x} \times (\nabla \times \mathbf{g}) dV - \frac{1}{n-1} \int_{\partial V} \mathbf{x} \times (\mathbf{n} \times \mathbf{g}) dS, \quad (\text{A1})$$

$$\int_V \nabla \zeta dV = -\frac{1}{n-1} \int_{\partial V} \mathbf{x} \times (\mathbf{n} \times \nabla \zeta) dS, \quad (\text{A2})$$

where \mathbf{x} is the position vector. These formulas are used in the derivation in Sec. III. And the results are independent of the origin of \mathbf{x} .

2. Generalized Reynolds transport theorem

The Newton–Leibniz formula in elementary calculus is

$$\frac{d}{dt} \int_{a(t)}^{b(t)} f(x, t) dx = \int_a^b \frac{\partial f}{\partial t} dx + \frac{db}{dt} f(b, t) - \frac{da}{dt} f(a, t). \quad (\text{A3})$$

This formula can be extended to multi-dimensional space. For a field quantity $\mathcal{H}(\mathbf{x}, t)$ in an arbitrary domain $D(t)$, of which the boundary $\partial D(t)$ may move and change shape over time with velocity \mathbf{v} , the generalized Reynolds transport theorem yields

$$\frac{d}{dt} \int_{D(t)} \mathcal{H}(\mathbf{x}, t) dV = \int_{D(t)} \frac{\partial \mathcal{H}}{\partial t} dV + \int_{\partial D(t)} \mathbf{n} \cdot \mathbf{v} \mathcal{H} dS. \quad (\text{A4})$$

In particular, if we want to trace \mathcal{H} in a material volume \mathcal{V} under the velocity $\mathbf{v} = \mathbf{u}$, then the above equation yields

$$\frac{d}{dt} \int_{\mathcal{V}} \mathcal{H} dV = \int_{\mathcal{V}} \left(\frac{d\mathcal{H}}{dt} + (\nabla \cdot \mathbf{u}) \mathcal{H} \right) dV. \quad (\text{A5})$$

For a fixed volume, $\mathbf{v} = \mathbf{0}$, then

$$\frac{d}{dt} \int_D \mathcal{H}(\mathbf{x}, t) dV = \int_D \frac{\partial \mathcal{H}}{\partial t} dV. \quad (\text{A6})$$

3. The derivation of impulse theory

Consider first the kinematic content of $\int_V \mathbf{a} dS$ in Eq. (14). For any genetic control volume V we have

$$\int_V \mathbf{a} dV = \frac{1}{n-1} \int_V \mathbf{x} \times (\nabla \times \mathbf{a}) dV - \frac{1}{n-1} \int_{\partial B + \Sigma} \mathbf{x} \times (\mathbf{n} \times \mathbf{a}) dS, \quad (\text{A7})$$

where

$$\nabla \times \mathbf{a} = \nabla \times \left(\frac{D\mathbf{u}}{Dt} \right) = \frac{D\boldsymbol{\omega}}{Dt} - \boldsymbol{\omega} \cdot \nabla \mathbf{u}. \quad (\text{A8})$$

For incompressible flow,

$$\begin{aligned} & -\frac{1}{n-1} \int_{\Sigma} \mathbf{x} \times (\mathbf{n} \times \mathbf{a}) dS \\ &= \frac{1}{n-1} \int_{\Sigma} \mathbf{x} \times \left[\mathbf{n} \times \left(\frac{\nabla p}{\rho} + \nu \nabla \times \boldsymbol{\omega} \right) \right] dS, \\ &= -\int_{\Sigma} \frac{p}{\rho} \mathbf{n} dS + \frac{1}{n-1} \int_{\Sigma} \mathbf{x} \times [\mathbf{n} \times (\nu \nabla \times \boldsymbol{\omega})] dS. \end{aligned} \quad (\text{A9})$$

so

$$\begin{aligned} \int_V \mathbf{a} dV &= \frac{1}{n-1} \int_V \mathbf{x} \times \left(\frac{D\boldsymbol{\omega}}{Dt} - \boldsymbol{\omega} \cdot \nabla \mathbf{u} \right) dV \\ & - \frac{1}{n-1} \int_{\partial B} \mathbf{x} \times (\mathbf{n} \times \mathbf{a}) dS - \int_{\Sigma} \frac{p}{\rho} \mathbf{n} dS \\ & + \frac{1}{n-1} \int_{\Sigma} \mathbf{x} \times [\mathbf{n} \times (\nu \nabla \times \boldsymbol{\omega})] dS. \end{aligned} \quad (\text{A10})$$

Substituting this equation into Eq. (14), we can obtain

$$\begin{aligned} \mathbf{F} &= -\frac{1}{n-1} \int_V \mathbf{x} \times \left[\frac{D(\rho \boldsymbol{\omega})}{Dt} - \rho \boldsymbol{\omega} \cdot \nabla \mathbf{u} \right] dV \\ & + \frac{1}{n-1} \int_{\partial B} \mathbf{x} \times (\mathbf{n} \times \rho \mathbf{a}) dS \\ & - \frac{1}{n-1} \int_{\Sigma} \mathbf{x} \times [\mathbf{n} \times (\mu \nabla \times \boldsymbol{\omega})] dS + \int_{\Sigma} \boldsymbol{\tau} dS. \end{aligned} \quad (\text{A11})$$

Since

$$\mathbf{x} \times (\boldsymbol{\omega} \cdot \nabla \mathbf{u}) = \begin{cases} 0, & \text{for } n = 2, \\ \nabla \cdot (\boldsymbol{\omega} \mathbf{x} \times \mathbf{u}) - \boldsymbol{\omega} \times \mathbf{u}, & \text{for } n = 3. \end{cases} \quad (\text{A12})$$

We can obtain

$$\begin{aligned}
 \mathbf{F} = & -\frac{1}{n-1} \int_V \mathbf{x} \times \frac{D(\rho\boldsymbol{\omega})}{Dt} dV - \frac{n-2}{n-1} \int_V \rho\boldsymbol{\omega} \times \mathbf{u} dV \\
 & + \frac{1}{n-1} \int_{\partial B} \mathbf{x} \times (\mathbf{n} \times \rho\mathbf{a}) dS + \frac{1}{n-1} \int_{\partial B} \mathbf{x} \times \rho\boldsymbol{\omega}_n dS \\
 & + \frac{1}{n-1} \int_{\Sigma} \mathbf{x} \times \rho\boldsymbol{\omega}_n dS + \frac{1}{n-1} \int_{\Sigma} (\mathbf{x} \times \rho\boldsymbol{\sigma} + \boldsymbol{\tau}) dS. \quad (A13)
 \end{aligned}$$

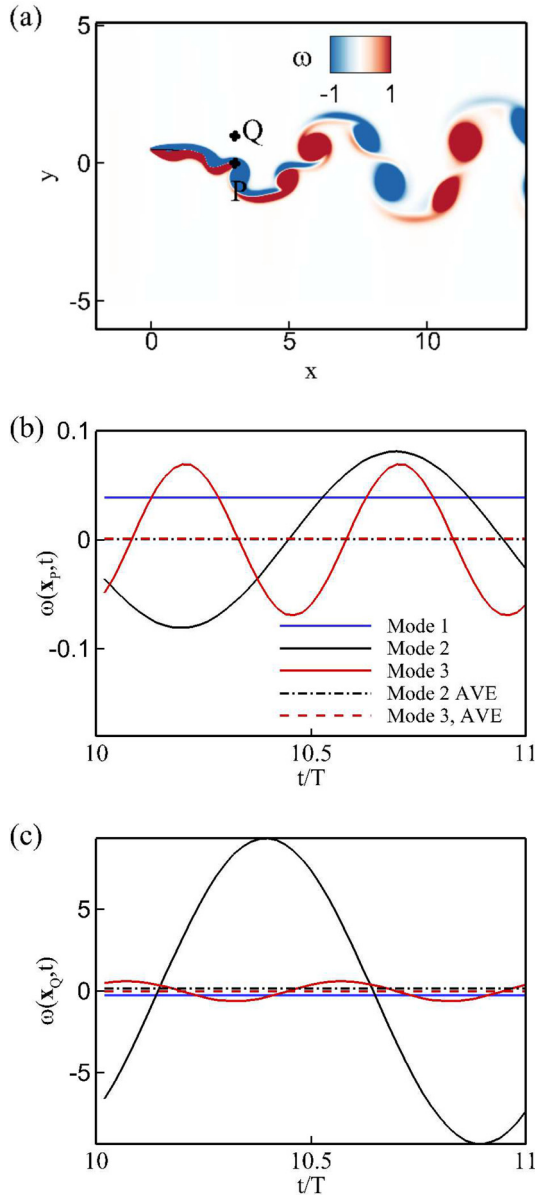


FIG. 17. (a) The vorticity contour for real flow at $t/T = 11$. P and Q are points fixed at x_P and x_Q . The time evolution of vorticity at point (b) x_P and (c) x_Q for mode 1, mode 2, and mode 3. The blue and red dashed lines are the time-averaged (AVE) vorticity value for mode 2 and 3, respectively.

For a generic fluid domain $V(t)$ with boundary velocity \mathbf{v} , by the generalized Reynolds transport formula [Eq. (A4)], the above equation can be rewritten as

$$\begin{aligned}
 \mathbf{F} = & -\frac{1}{n-1} \frac{d}{dt} \int_V \mathbf{x} \times \rho\boldsymbol{\omega} dV - \frac{1}{n-1} \int_{\Sigma} (\mathbf{x} \times \rho\boldsymbol{\omega})(\mathbf{u} - \mathbf{v}) \cdot \mathbf{n} dS \\
 & - \int_V \rho\boldsymbol{\omega} \times \mathbf{u} dV + \frac{1}{n-1} \int_{\partial B} \mathbf{x} \times (\mathbf{n} \times \rho\mathbf{a}) dS \\
 & + \frac{1}{n-1} \int_{\partial B} \mathbf{x} \times \rho\boldsymbol{\omega}_n dS + \frac{1}{n-1} \int_{\Sigma} \mathbf{x} \times \rho\boldsymbol{\omega}_n dS \\
 & + \frac{1}{n-1} \int_{\Sigma} (\mathbf{x} \times \rho\boldsymbol{\sigma} + \boldsymbol{\tau}) dS. \quad (A14)
 \end{aligned}$$

APPENDIX B: TIME EVOLUTION OF VORTICITY FIELD FOR EACH MODE

In order to analyze the force contributed by each mode, it is important to comprehend the temporal behavior of vorticity for each DMD mode. Figures 17(b) and 17(c) show the time evolution of vorticity at two fixed points for mode 1, mode 2, and mode 3. It has been observed that, apart from mode 1 which exhibits a nonzero time-averaged vorticity value, the vorticity at each Euler point undergoes sinusoidal oscillations over time, with a time-averaged value of zero.

REFERENCES

- ¹P. J. Schmid, "Dynamic mode decomposition of numerical and experimental data," *J. Fluid Mech.* **656**, 5–28 (2010).
- ²K. Menon and R. Mittal, "Dynamic mode decomposition based analysis of flow over a sinusoidally pitching airfoil," *J. Fluids Struct.* **94**, 102886 (2020).
- ³S. L. Brunton and B. R. Noack, "Closed-loop turbulence control: Progress and challenges," *Appl. Mech. Rev.* **67**, 050801 (2015).
- ⁴D. Sipp, O. Marquet, P. Meliga, and A. Barbagallo, "Dynamics and control of global instabilities in open-flows: A linearized approach," *Appl. Mech. Rev.* **63**, 030801 (2010).
- ⁵J. Q. Kou and W. W. Zhang, "Dynamic mode decomposition and its applications in fluid dynamics," *Acta Aerodyn. Sin.* **36**, 163–179 (2018).
- ⁶B. Wu, C. Shu, H. Lee, and M. Wan, "The effects of caudal fin's bending stiffness on a self-propelled carangiform swimmer," *Phys. Fluids* **34**, 041901 (2022).
- ⁷Y. Zeng, Y. Wang, T. Wang, and Q. Chen, "Numerical study on flow-induced vibrations of elastically mounted rectangular cylinders without and with barrier walls," *Phys. Fluids* **34**, 083613 (2022).
- ⁸M. Grilli, P. J. Schmid, S. Hickel, and N. A. Adams, "Analysis of unsteady behaviour in shockwave turbulent boundary layer interaction," *J. Fluid Mech.* **700**, 16–28 (2012).
- ⁹J. Q. Kou and W. W. Zhang, "Dynamic mode decomposition with exogenous input for data-driven modeling of unsteady flows," *Phys. Fluids* **31**, 057106 (2019).
- ¹⁰H. F. Zhang, L. Zhou, T. T. Liu, Z. J. Guo, and F. Golnary, "Dynamic mode decomposition analysis of the two-dimensional flow past two transversely in-phase oscillating cylinders in a tandem arrangement," *Phys. Fluids* **34**, 033602 (2022).
- ¹¹J. M. Burgers, "On the resistance of fluids and vortex motion," *Proc. K. Ned. Akad. Wet., Ser. B* **23**, 774–782 (1921).
- ¹²J. C. Wu, "Theory for aerodynamic force and moment in viscous flows," *AIAA J.* **19**, 432–441 (1981).
- ¹³M. J. Lighthill, *An Informal Introduction to Theoretical Fluid Mechanics* (Clarendon Press, Oxford, 1986).
- ¹⁴C. C. Chang, "Potential flow and forces for incompressible viscous flow," *Proc. R. Soc. A* **437**, 517–525 (1992).
- ¹⁵F. Noca, D. Shiels, and D. Jeon, "A comparison of methods for evaluating time-dependent fluid dynamic forces on bodies, using only velocity fields and their derivatives," *J. Fluids Struct.* **13**, 551–578 (1999).

- ¹⁶J. Z. Wu, H. Y. Ma, and M. Zhou, *Vorticity and Vortex Dynamics* (Springer, 2006).
- ¹⁷L. L. Kang, L. Q. Liu, W. D. Su, and J. Z. Wu, “Minimum-domain impulse theory for unsteady aerodynamic force,” *Phys. Fluids* **30**, 016107 (2018).
- ¹⁸J. Li and Z.-N. Wu, “Vortex force map method for viscous flows of general airfoils,” *J. Fluid Mech.* **836**, 145–166 (2018).
- ¹⁹G.-J. Li and X.-Y. Lu, “Force and power of flapping plates in a fluid,” *J. Fluid Mech.* **712**, 598–613 (2012).
- ²⁰W. Tong, Y. Yang, and S. Wang, “Estimating thrust from shedding vortex surfaces in the wake of a flapping plate,” *J. Fluid Mech.* **920**, A10 (2021).
- ²¹M. Gazzola, M. Argentina, and L. Mahadevan, “Scaling macroscopic aquatic locomotion,” *Nat. Phys.* **10**, 758–761 (2014).
- ²²K. Liu, X. C. Liu, and H. B. Huang, “Scaling the self-propulsive performance of pitching and heaving flexible plates,” *J. Fluid Mech.* **936**, A9 (2022).
- ²³L.-M. Chao, M. M. Alam, and L. Cheng, “Hydrodynamic performance of slender swimmer: Effect of travelling wavelength,” *J. Fluid Mech.* **947**, A8 (2022).
- ²⁴Z.-R. Peng, Y. Sun, D. Yang, Y. Xiong, L. Wang, and L. Wang, “Scaling laws for drag-to-thrust transition and propulsive performance in pitching flexible plates,” *J. Fluid Mech.* **941**, R2 (2022).
- ²⁵L. L. Kang, W. C. Cui, X.-Y. Lu, and H. B. Huang, “Hydrodynamic force induced by vortex–body interactions in orderly formations of flapping tandem flexible plates,” *Phys. Fluids* **34**, 021901 (2022).
- ²⁶Z. Muhammad, M. M. Alam, and B. R. Noack, “Efficient thrust enhancement by modified pitching motion,” *J. Fluid Mech.* **933**, A13 (2022).
- ²⁷S. Chen and G. D. Doolen, “Lattice Boltzmann method for fluid flows,” *Annu. Rev. Fluid Mech.* **30**, 329–364 (1998).
- ²⁸Z. Guo, B. Shi, and N. Wang, “Lattice BGK model for incompressible Navier–Stokes equation,” *J. Comput. Phys.* **165**, 288–306 (2000).
- ²⁹J. F. Doyle and E. Desantiago, “Nonlinear analysis of thin-walled structures: Statics, dynamics, and stability. Mechanical engineering series,” *Appl. Mech. Rev.* **55**, B92 (2002).
- ³⁰D. Goldstein, R. Handler, and L. Sirovich, “Modeling a no-slip flow boundary with an external force field,” *J. Comput. Phys.* **105**, 354–366 (1993).
- ³¹R.-N. Hua, L. Zhu, and X.-Y. Lu, “Dynamics of fluid flow over a circular flexible plate,” *J. Fluid Mech.* **759**, 56–72 (2014).
- ³²C. Tang, N.-S. Liu, and X.-Y. Lu, “Dynamics of an inverted flexible plate in a uniform flow,” *Phys. Fluids* **27**, 073601 (2015).
- ³³L. L. Kang, X. Y. Lu, and W. C. Cui, “Intermittent swimming of two self-propelled flapping plates in tandem configuration,” *Phys. Fluids* **34**, 011905 (2022).
- ³⁴Z.-R. Peng, H. B. Huang, and X.-Y. Lu, “Collective locomotion of two closely spaced self-propelled flapping plates,” *J. Fluid Mech.* **849**, 1068–1095 (2018).
- ³⁵L. L. Kang, Z.-R. Peng, H. B. Huang, X.-Y. Lu, and W. C. Cui, “Active external control effect on the collective locomotion of two tandem self-propelled flapping plates,” *Phys. Fluids* **33**, 101901 (2021).
- ³⁶X.-G. Luo, A.-K. Gao, and X.-Y. Lu, “Enhanced performance of a self-propelled flexible plate by a uniform shear flow and mechanism insight,” *Phys. Fluids* **35**, 021903 (2023).
- ³⁷L. L. Kang, A.-K. Gao, F. Han, W. C. Cui, and X.-Y. Lu, “Propulsive performance and vortex dynamics of jellyfish-like propulsion with burst-and-coast strategy,” *Phys. Fluids* **35**, 091904 (2023).
- ³⁸Q. X. Huang, J. Q. Kou, F.-B. Tian, J. Young, J. Lai, and S. Ravi, “Dynamic mode decomposition for unsteady flow over flapping wings,” AIAA Paper No. AIAA 2023-1618, 2023.
- ³⁹X. J. Zhu, G. W. He, and X. Zhang, “Flow-mediated interactions between two self-propelled flapping filaments in tandem configuration,” *Phys. Rev. Lett.* **113**, 238105 (2014).